Journal of Geophysical Research: Atmospheres

RESEARCH ARTICLE
10.1029/2017JD028060

Characteristics of Water Vapor Turbulence Profiles in Convective Boundary Layers During the Dry and Wet Seasons Over Darwin

M. K. Osman[1], D. D. Turner[2], T. Heus[3], and R. Newsom[4]

[1]Cooperative Institute for Mesoscale Meteorological Studies, The University of Oklahoma, and NOAA/National Severe Storms Laboratory, Norman, OK, USA, [2]NOAA Earth System Research Laboratory, Global Systems Division, Boulder, CO, USA, [3]Department of Physics, Cleveland State University, Cleveland, OH, USA, [4]Pacific Northwest National Laboratory, Richland, WA, USA

Key Points:
- Analysis of water vapor turbulence profiles was performed for the wet and dry season cases separately
- Comparisons of turbulent statistics revealed that the dry season is more comparable to observations in Oklahoma than to the wet season
- The dry season showed deeper CBL, larger gradient of water vapor mixing at z_i, and smaller variance

Correspondence to:
M. K. Osman,
mohammed.osman@noaa.gov

Citation:
Osman, M. K., Turner, D. D., Heus, T., & Newsom, R. (2018). Characteristics of water vapor turbulence profiles in convective boundary layers during the dry and wet seasons over Darwin. *Journal of Geophysical Research: Atmospheres*, *123*, 4818–4836. https://doi.org/10.1029/2017JD028060

Received 14 NOV 2017
Accepted 9 APR 2018
Accepted article online 23 APR 2018
Published online 17 MAY 2018

Abstract This study explores water vapor turbulence in the convective boundary layer (CBL) using the Raman lidar observations from the Atmospheric Radiation Measurement site located at Darwin, Australia. An autocovariance technique was used to separate out the random instrument error from the atmospheric variability during time periods when the CBL is cloud-free, quasi-stationary, and well mixed. We identified 45 cases, comprising of 8 wet and 37 dry seasons events, over the 5-year data record period. The dry season in Darwin is known by warm and dry sunny days, while the wet season is characterized by high humidity and monsoonal rains. The inherent variability of the latter resulted in a more limited number of cases during the wet season. Profiles of the integral scale, variance, coefficient of the structure function, and skewness were analyzed and compared with similar observations from the Raman lidar at the Atmospheric Radiation Measurement Southern Great Plains (SGP) site. The wet season shows larger median variance profiles than the dry season, while the median profile of the variance from the dry season and the SGP site are found to be more comparable particularly between 0.4 and 0.75 z_i. The variance and coefficient of the structure function show qualitatively the same vertical pattern. Furthermore, deeper CBL, larger gradient of water vapor mixing ratio at z_i, and the strong correlation with the water vapor variance at z_i are seen during the dry season. The median value in the skewness is mostly positive below 0.6 z_i unlike the SGP site.

1. Introduction

The lowest portion of the atmosphere that is directly influenced by its contact with the Earth's surface is called atmospheric boundary layer. During the daytime, solar heating of the surface drives convective mixing in the atmospheric boundary layer; this is also called the convective boundary layer (CBL). Its thickness is quite variable both in space and time, ranging from tens of meters to 4 km or more (e.g., McGrath-Spangler & Denning, 2013; Neves & Fisch, 2015; Turner, Wulfmeyer, et al., 2014; this work). Turbulence is ubiquitous throughout the CBL and plays an important role in redistributing trace gases, aerosols, heat, and momentum. The vertical profiles of turbulent fluctuations of water vapor are critical in understanding the structure of the CBL since turbulence in the CBL is often described by its statistical properties including the vertical profiles of water vapor mean (first moment), variance (second moment), and skewness (third moment). Water vapor mixing ratio is a good atmospheric tracer gas as it is a conserved quantity under adiabatic conditions and in the absence of condensation and evaporation. The profile of water vapor variance is also an important parameter in many turbulence, convection, and cloud parameterizations (Berg & Stull, 2005; Tompkins, 2002). It increases with height, reaching its peak value at the top of the CBL due to the intensive mixing of moist air being lofted from the CBL into the free troposphere and the drier air descending from the free troposphere into the CBL. Furthermore, the profile of water vapor skewness offers insight into the vertical transport of water vapor through the top of the CBL (e.g., Couvreux et al., 2005). Hence, proper representation of these turbulent processes in models is needed to improve both climate simulations and weather forecasts.

In order to evaluate and improve turbulence parameterizations in weather and climate models, high resolution and accurate measurements of profiles of turbulence throughout the CBL are needed. Vertical profiles of turbulent motion have been studied using various types of instruments including in situ aircraft measurement (Albrecht et al., 1995; Andrews et al., 2004; Lenschow et al., 1980; Stull et al., 1997;

Vogelmann et al., 2012; Williams & Hacker, 1992), radiosonde soundings (Cooper & Eichinger, 1994; Frehlich & Sharman, 2010; Garcia-Carreras et al., 2015; Neves & Fisch, 2015; Wilson et al., 2011), wind profiling radars (Angevine et al., 1994; Cohn, 1995; Dehghan et al., 2014; Ecklund et al., 1988; McCaffrey, Bianco, & Wilczak, 2016; McCaffrey, Bianco, Johnston, et al., 2016; Strauch et al., 1984; White et al., 1991), and tall towers (Businger et al., 1971; Kaimal & Gaynor, 1983; van Ulden & Wieringa, 1996; Wilczak & Tillman, 1980). Even though tall towers can take measurements continuously for long periods of time, their vertical coverage is limited to the lowest portion of the CBL due to their limited height. Aircraft measurements have their disadvantages because the measurements cannot be taken throughout the CBL simultaneously, and thus, there can be uncertainties associated with relating the turbulent moments to the height of the CBL (Turner, Ferrare, et al., 2014), and the expense of flying aircraft prohibits collecting measurements for extended periods of time. Radiosondes offer a snapshot of the CBL profiles, are unable to profile at very high (~1 min) resolution, and too expensive to take continuous measurements for an extended period of time. Wind profiling radars operate continuously in nearly all-weather conditions; however, lidars provide routine, continuous measurements at all altitudes throughout the CBL with better temporal and spatial resolutions albeit with limited profiling capability in clouds. This makes lidars an outstanding tool for studying the small-scale turbulent structure of the CBL under different atmospheric conditions.

Different kinds of lidars have been used to study turbulence in the CBL. McNicholas and Turner (2014) used high spectral resolution lidar aerosol backscatter coefficient measurements from Oklahoma (USA) to study turbulent motion in the CBL. The authors were able to calculate up to the forth-order moments using 17 cloud-free 2-hr periods cases during which the CBL was stationary. They showed the non-Gaussian nature of turbulence at the top of the CBL from the comparisons between the skewness and kurtosis. Lenschow et al. (2000) also showed the capability of high-resolution Doppler lidar to measure turbulence statistics of vertical velocity by calculating the profiles second- through fourth-order moments of vertical wind velocity throughout most of the CBL. The authors compared the results with large-eddy simulations (LESs) and found that atmospheric stability was a key factor for the observed variability in the vertical profiles of higher order moments from one case to another. Bonin et al. (2016) studied vertical velocity statistics using Doppler lidars and found the vertical velocity variance from Doppler lidars to be in good agreement with sonic anemometer measurements on a 300-m tower. Berg, Newsom, and Turner (2016) analyzed 1 year of Doppler lidar measurements of the vertical velocity in the cloud-free CBL over the SGP site, evaluating how these profiles evolve from sunrise to sunset, the seasonal differences in the CBL evolution, and their sensitivity to wind direction, surface shear stress, degree of instability in the CBL, and wind shear across the top of the CBL. Water vapor differential absorption lidars (Behrendt et al., 2011; Giez et al., 1999; Kiemle et al., 1997; Muppa et al., 2016; Wulfmeyer, 1999a, 1999b) and water vapor Raman lidars (Wulfmeyer et al., 2010; Turner, Ferrare, et al., 2014; Turner, Wulfmeyer, et al., 2014) have also been utilized to characterize turbulence structure in the CBL.

Most previous lidar studies of turbulence in the CBL have been based on a limited number of cases, which restricts the representativeness of the results for different atmospheric conditions. Turner, Wulfmeyer, et al. (2014) presented the first long-term data set of water vapor variance and skewness profiles in the CBL using more than 6 years of water vapor data for different seasons and atmospheric conditions. The authors identified 300 afternoon cases that were observed by the Raman lidar at the Atmospheric Radiation Measurement (ARM) Southern Great Plains (SGP; Sisterson et al., 2016) during which the CBL was quasi-stationary and well mixed, derived vertical profiles of variance and skewness from these cases, and evaluated the correlation of these profiles with other parameters. Such large data sets will be very useful for evaluating and improving turbulence parameterization schemes used in cloud resolving, general circulation, and climate models.

The objective of this study is to explore the water vapor turbulence in the CBL over the tropics. Turbulence in the tropics has not yet been well studied compared to the midlatitudes, and its boundary layer dynamics are fundamentally different from the midlatitude dynamics. One important difference between them is the monsoon circulation, which is a continental scale event driven by the contrast in the thermal properties between the land and ocean surfaces (Holton, 2004), which leads to seasonal changes in much of the tropics. This circulation is accompanied by a reversal of the prevailing wind direction and an enhanced monsoon

rainfall. The atmospheric monsoonal circulation in northern Australia not only transports moist maritime air masses from the tropical Indian Ocean to northern Australia but also causes more than 85% of the annual rainfall in the area (Bowman et al., 2010). This gives an opportunity to compare the profiles of water vapor turbulence for the monsoon (wet season) and nonmonsoon (dry season) and see the effect of monsoonal circulation on the boundary layer water vapor turbulence. This study is unique because it uses for the first time a large Raman lidar water vapor data set from the tropics, where there are limited ground-based remote sensing measurements.

Data from the Raman lidar that measures of water vapor over the ARM Tropical Western Pacific (TWP) site located at Darwin, Australia (12.4°S, 130.9°E; Long et al., 2016) have been used in this study. This data set spans 5 years from December 2010 to December 2015. The Raman lidar used in this study had exactly the same specifications as the Raman lidar at the SGP site that has been shown to have the required accuracy and noise level to measure the second- and third-order moments of the water vapor mixing ratio in the CBL (Turner, Wulfmeyer, et al., 2014; Wulfmeyer et al., 2010).

Our study examines profiles of water vapor turbulence during which the CBL is cloud-free, quasi-stationary, and well mixed over a 2-hr period. We identified 45 afternoon cases, consisting of 8 wet and 37 dry seasons events, over the 5-year data record. Wet and dry season cases were treated separately to derive the median second- and third-order moments along with the integral scale (IS) and coefficient of the structure function. We found striking differences in these variables among the tropical wet season, dry season, and midlatitude cases.

The rest of the paper is organized as follows. A description of the Raman lidar that we used in this study is presented in section 2. Section 3 describes our selection of cases and our use of the autocovariance technique, as well as how we identified and removed outliers. Section 4 discusses the turbulence statistics results including IS, variance, the coefficient of the structure function, and skewness along with their corresponding noise and sampling error profiles. Comparison between the turbulence statistics from this study and the midlatitude data that were obtained from Turner, Wulfmeyer, et al. (2014) are discussed in section 5. The summary and concluding remarks of the study are given in section 6.

2. The Darwin Raman Lidar

The Raman lidar at Darwin is almost identical to the SGP Raman lidar, which is described in Goldsmith et al. (1998) and Turner, Goldsmith, and Ferrare (2016). The lidar uses a pulsed Nd:YAG laser to transmit approximately 350-mJ pulses of laser energy at 355 nm into the atmosphere at 30 Hz. Backscattered energy is collected with a 24-inch telescope, which then encounters a wedged beam splitter that directs approximately 5% of the energy into a set of wide field-of-view (FOV, 2 mrad) channels with the remaining energy going to a set of narrow FOV (NFOV, 300 μrad) channels. Each FOV uses dichroic beam splitters and photomultiplier tubes to separate and measure backscattered energy at 408 and 387 nm (Raman scattering by water vapor and nitrogen molecules, respectively) and at the laser wavelength simultaneously. The NFOV also has channels to measure the rotational Raman scattering by nitrogen and oxygen (at 353 and 354 nm) and the cross-polarization return (relative to the laser's polarization). All measurements are made at a resolution of 7.5 m, 10 s; however, generally, the resolution is decreased in postprocessing to improve the signal-to-noise ratio. The Raman lidar's detection electronics uses both analog-to-digital and photon-counting in each channel (Newsom et al., 2009).

Similar to Turner, Wulfmeyer, et al. (2014), this study uses only the water vapor mixing ratio derived from the NFOV water vapor and nitrogen Raman scattering observations. First, the raw analog voltage and photon counting signals are merged through a process called "gluing" (Newsom et al., 2009). Gluing is the process of combining the analog and photon counting data together (Whiteman et al., 2006). Then the merged counting rate data are averaged to 37.5 m in the vertical, while maintaining the temporal resolution at 10 s. After removing the background from each of the combined water vapor and nitrogen backscatter profiles, the ratio of the profiles is computed and an overlap correction is applied; this profile is now proportional to the water vapor mixing ratio. The data are calibrated using water vapor mixing ratio obtained from radiosondes. Additional details on the method used to derive the water vapor mixing ratio profile are provided in Turner and Goldsmith (1999). The ARM Raman lidar water vapor mixing ratio data set was used in the study (ARM Climate Research Facility, 2004).

3. Lidar Data and Analysis Method

Raman lidar data are inherently noisy and thus proper lidar data analysis requires separation of the instrument noise from the true atmospheric measurements. Therefore, we first present the autocovariance technique that was used to remove the instrument noise following the discussion of criteria for selecting the cases and removing the outliers from the chosen data set.

3.1. Data Set Selection Criteria

While the Darwin Raman lidar was an operational lidar and designed to run continuously, it did experience significant periods of downtime due to laser and mechanical issues. The data used in this study were manually screened by looking at the time-height cross sections of water vapor mixing ratio to identify afternoons during which the CBL was quasi-stationary and well mixed for at least 2 hr. In particular, afternoons during which there were large changes in the synoptic conditions were removed. There were several cases where the instrument noise variance at the top of the CBL was much larger than the true atmospheric variance at the same height (see section 3.3 how we separate instrumental and atmospheric variance from total variance), and in these situations, the random errors in the derived variance and the third-order moment profiles were quite large. Consequently, we required the atmospheric variance of water vapor mixing ratio at the top of the CBL be at least 30% of the total variance at the same height; this is consistent with Turner, Wulfmeyer, et al. (2014). This resulted in 45 cases, consisting of 8 wet and 37 dry season events, over the 5-year data record. Each case had the same period (2 hr) so that the sampling errors were roughly equivalent for all cases.

Our very restrict case selection criteria (i.e., cloud-free, quasi-stationary, and well mixed for at least 2 hr) limited the number of cases we could analyze particularly for the wet season because these atmospheric conditions are not common at Darwin site during the wet season. These selection criteria are used because we need to analyze a time series instead of a spatial field. The choice of starting with cloud-free days is twofold. First, boundary layer parameterizations must be able to represent clearly sky mixing properly, which arguably is simpler than cloudy boundary layer conditions. Second, we chose to focus on cloud-free days so statistical moments could be derived throughout the CBL. The presence of cloud makes the removal of the instrument noise from atmospheric measurements difficult since lidar observations above cloud base are inherently noisy. As a result, the lidars' capability of resolving the vertical structure of turbulence at the top of the CBL and especially the accurate computation of the second- and third-order moments are much more difficult in cloud-topped CBLs.

3.2. Identification and Removal of Outliers

In order to apply the autocovariance technique to separate out the instrument noise from the atmospheric variability, outliers first need to be removed from water vapor time series at every altitude in each of the 2-hr periods. Since the distribution of water vapor at a given level in the 2-hr period is not necessarily symmetric, we followed the split-histogram approach developed by McNicholas and Turner (2014) to remove outliers using three standard deviations in this work. The quality control threshold profiles were smoothed with height. The threshold profiles were different for different cases since each 2-hr data set was treated independently. The number of outliers removed from each altitude was typically less than 2%, and often, the removed data points were above the CBL. We used linear interpolation to replace the removed outliers. Following the removal of outliers and filling gaps, the time series at each altitude was linearly detrended after subtracting the mean. This resulted in a time series of water vapor turbulent fluctuations $q'(t)$ plus the instrument noise ϵ, that is, $q'(t)+\epsilon$ (see equation (1)) with a mean of zero at each height. At this stage, we can apply the autocovariance technique to remove the instrument noise and analyze the time series of water vapor turbulent fluctuations.

3.3. Autocovariance Technique

Lidar observed water vapor mixing ratio q at each altitude within the CBL reads as

$$q = \overline{q} + q' + \epsilon \tag{1}$$

where $\overline{q}$ is the mean water vapor mixing ratio, q' is turbulent fluctuation of water vapor mixing ratio, and ϵ is uncorrelated instrument noise. Before vertical profiles of the turbulent fluctuations of water vapor mixing ratio can be derived from the lidar observations, it is necessary to separate the noise from the true

atmospheric variability. There are different techniques available to do this, but the autocovariance technique outlined by Lenschow et al. (2000) is perhaps the most efficient and straightforward to implement. This technique is based on the assumption that atmospheric fluctuations are correlated in time, while instrumental noise fluctuations are uncorrelated, and hence, instrument noise will not contribute to the autocovariance function at lags larger than zero. The autocovariance of a time series with itself at lag zero will then be the total variance of the observations, which is the sum of the true atmospheric variance and the instrument noise variance. And their relationship is expressed as

$$\overline{\epsilon^2} = M_{11}(0) - M_{11}(\rightarrow 0) = M_{11}(0) - \overline{q'^2} \tag{2}$$

where $\overline{\epsilon^2}$ is the instrument noise variance, $M_{11}(\tau)$ is the autocovariance function at lag τ, and $M_{11}(\rightarrow 0)$ indicates the extrapolation of M_{11} to lag zero, which corresponds to the true atmospheric variance of water vapor mixing ratio $\overline{q'^2}$. Assuming that the atmospheric variance, $\overline{q'^2}$, is mainly as a result of isotropic turbulence within inertial subrange (Monin & Yaglom, 1979), $M_{11}(\tau)$ can be approximated by the structure function as

$$M_{11}(\tau) = \overline{q'^2} - C\tau^{2/3} \tag{3}$$

where C is a parameter that contains both the eddy dissipation and the scalar variance dissipation since q' is a scalar and τ is the time lag. We utilized equations (2) and (3) to get the profiles of instrument noise variance, the atmospheric variance, and coefficient of the structure function (i.e., C). In this study, we used 15 data points covering 150 s to extrapolate back to lag zero using the structure function shown in equation (3). We found this number of data points to be most effective, and this same number of points was also used in previous studies such as Van Weverberg et al. (2016) and Behrendt et al. (2015). In fact, we examined the results for different number of fit lags (i.e., 8 and 10) and found that the number of data points used does not affect the results significantly.

Since the theoretical shape of the third-order autocovariance function in the inertial subrange is not known, the approximate value of $M_{21}(\rightarrow 0)$ was obtained from the mean of M_{21} at lags one through five in order to separate out the instrument noise from the true third-order moment. In fact, similar results were obtained using a linear fit to extrapolate the autocovariance functions to zero lag.

Subsequently, the skewness S was computed from the third-order moment and variance as

$$S = \frac{\overline{q'^3}}{\overline{q'^2}^{3/2}} \tag{4}$$

where $\overline{q'^3}$ is third-order moment. We calculated the IS, which measures the amount of time that the turbulence is correlated with itself, as follows:

$$\mathrm{IS} = \frac{1}{\overline{q'^2}} \int_0^{\tau_0} M_{11}(\tau) d\tau \tag{5}$$

where τ_o is the first zero crossing of the autocovariance function. The IS provides information about the capability of lidar to resolve the turbulent water vapor fluctuations including the major part of the inertial subrange throughout the CBL; this happens if the IS is much larger than the temporal resolution of the observations of the lidar.

The noise and sampling errors in the variance, third-order moment, skewness, and IS were computed in order to provide the uncertainty associated with these variables. The methods outlined in Lenschow et al. (2000) were utilized to compute the noise errors, the sampling errors in the variance and third moment were computed using the method provided in Lenschow et al. (1994), and the sampling error in the skewness was calculated using the technique found in Mann et al. (1995). While the noise error calculations involve the atmospheric and instrument noise variances, the sampling errors were computed using the IS for 2-hr time series.

4. Atmospheric Statistical Results

This section is devoted to characterizing the turbulence profiles obtained from the ARM Raman lidar water vapor measurements made over Darwin from December 2010 to December 2015. This continuous long-term data set not only allows us to compute profiles of the median and other percentiles of the variance,

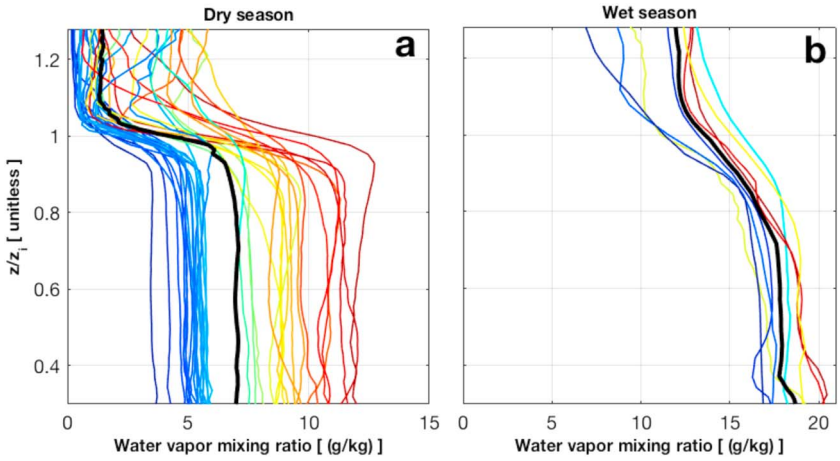

Figure 1. Mean water vapor mixing ratio profiles for each 2-hr period for the (a) dry season and (b) wet season with 37 and 8 cases, respectively. The blue through red colors correspond lowest to highest mixing ratio values at 0.3 z_i. The solid black lines are the median profiles in the wet and dry season periods.

coefficient of the structure function, skewness, and IS from the large data set but also enables us to examine how these turbulent profiles change under different atmospheric conditions. Furthermore, since the TWP Raman lidar had similar specifications as the Raman lidar at the SGP site, we have the opportunity to compare our turbulent statistics with similar observations obtained in midlatitudes. Since the heights of the top of the CBL (z_i, the altitude aboveground level where the variance of water vapor reaches its maximum value) varied over the 45 cases, the turbulent profiles of each of the cases were interpolated to a common normalized height grid (i.e., z/z_i). This enables us to properly compare the profiles and compute median and other percentiles for each altitude.

4.1. Mean Water Vapor Mixing Ratio

Figure 1 shows the vertical profiles of the mean water vapor mixing ratio (g kg^{-1}) for each 2-hr case obtained over Darwin separated into dry and wet season events. The vertical axes have been normalized by the CBL depth, z_i. The wet season in Darwin, ranging from November to April, is characterized by high humidity, monsoonal rains, and storms, while the dry season is, from May until October, known by warm, dry sunny days, and cool nights (e.g., Drosdowsky, 1996; Evans et al., 2012; Holland, 1986; Pope et al., 2008). Since April, October, and November are considered buildup or transitional seasons, they have been removed from the analysis. Besides rainfall, the Australian seasons can also be described based on a wind definition (e.g., Murakami, Iwashima, & Nakasawa, 1984; Murakami & Sumi, 1982; Troup, 1961). In Darwin, during the dry season, the wind predominantly blows southeasterly, while in the wet season, it is mostly westerly or northwesterly.

In Figure 1, the colors blue through red correspond to lowest to highest water vapor mixing ratios for the wet and dry seasons at height 0.3 z_i. The black thick lines in Figure 1 indicate the median of water vapor mixing ratio profiles at Darwin for the wet and dry season periods. The median profiles were computed from 8 and 37 cases for wet and dry season events, respectively. Figure 1 clearly shows that the median of water vapor mixing ratio in the wet season is higher than the dry season case, which is consistent with the characteristics of the seasons, that is, humid air in the wet season and dry air in dry season. The same figure reveals that the water vapor mixing ratios are nearly constant from 0.3 to 0.8 z_i (which is expected in well mixed CBLs) and decreases above 0.8 z_i due to entrainment of drier air from the free troposphere. Consequently, the sharpest vertical gradient in water vapor mixing ratio profiles occurs at about z_i. In fact, the profiles of water vapor during the dry season decrease faster than wet season profiles above the top of the CBL. In the wet season, not only are high water vapor levels observed in the free troposphere but also the vertical gradient of profiles of water vapor at z_i is smaller than in the dry season. One likely reason for these is a monsoonal atmospheric circulation in the northern Australian continent where predominantly westerly or northwesterly wind brings moist maritime air masses from the tropical Indian Ocean to Darwin. Furthermore, Holloway and Neelin (2009) showed generally enhanced moisture in the free troposphere, rather than in the boundary layer,

Table 1
The 10th, 25th, 50th, 75th, and 90th Percentiles of the Variance of Water Vapor Mixing Ratio ($g^2\ kg^{-2}$) at the Top of the CBL and the Depth of the CBL (km) Derived From the Wet and Dry Season Cases

	Variance $[(g/kg)^2]$ at z_i						z_i (km)	
	Wet season			Dry season				
Percentile	Measured value	Random uncertainty	Sampling uncertainty	Measured value	Random uncertainty	Sampling uncertainty	Wet season	Dry season
10th	0.49	0.01	0.09	0.53	0.01	0.07	0.86	1.42
25th	0.86	0.01	0.14	0.82	0.01	0.12	0.96	1.51
Median	1.54	0.02	0.26	1.27	0.01	0.19	1.07	1.67
75th	2.07	0.02	0.32	2.45	0.03	0.45	1.35	1.99
90th	2.99	0.02	0.45	3.32	0.04	0.54	2.12	2.16

Note. The percentiles of the random and sampling uncertainties of the variance are displayed in Table 1, while the uncertainty in z_i is considered to be 37.5 m which is the vertical resolution of the Raman lidar data used in this analysis.

with increasing rainfall. Another possible reason for the absence of a sharp gradient near z_i in the wet season is strong turbulent mixing due to a relatively large dissipation rate generated by small eddies. The size of an eddy at z_i is proportional to the depth of the CBL, and the wet season generally has shallow CBL depth as shown in Table 1, which will be discussed later in this section. We also found an overall smaller ratio of the entrainment zone thickness to the CBL depth during the dry season than the wet season, suggesting that the sharper water vapor mixing ratio in the entrainment zone during the dry season is related with deeper CBL. The thickness of the entrainment zone is roughly estimated using the full width at half maximum distance across the largest value of the variance profile. The discussion of the CBL depth and the relationship between dissipation rate and size of eddies follows in the current section.

4.2. Distribution of the Center of the 2-hr Period, the CBL Depth, and Integral Scale at z_i

The distributions of the time-of-day of the center of the 2-hr period, the height of the top of the CBL, and the integral time scale at the top of the CBL for the wet and dry seasons are shown in Figure 2. The local time in Darwin is UTC + 0930, so the sunset is about 0930 UTC and solar noon is around 0300 UTC. Figure 2a shows that the center of the 2-hr periods, during which the CBL was quasi-stationary and well mixed, occurred after the local noon and before the sunset. The same figure reveals that the center of the 2-hr periods tends to occur mostly in the late afternoon during the wet season and that the dry season shows a wider spread in the center time of the 2-hr periods. Figure 2b demonstrates that the CBL in the wet season is shallow, and it is deeper during the dry season as expected. This is due to the fact that there are relatively larger latent heat fluxes during the wet season, yet the sensible heat fluxes are relatively larger during the dry season (Chan & Wood, 2013). The median CBL heights are 1,070 and 1,670 m altitude aboveground level in the wet and dry season periods, respectively. Figure 2c shows that the IS at the top of the CBL ranges between 40 and 140 s. This is much larger than the temporal resolution of the Raman lidar (10 s), suggesting that the lidar is able to resolve the major part of the turbulent fluctuations of the CBL. The distribution of IS during the dry season

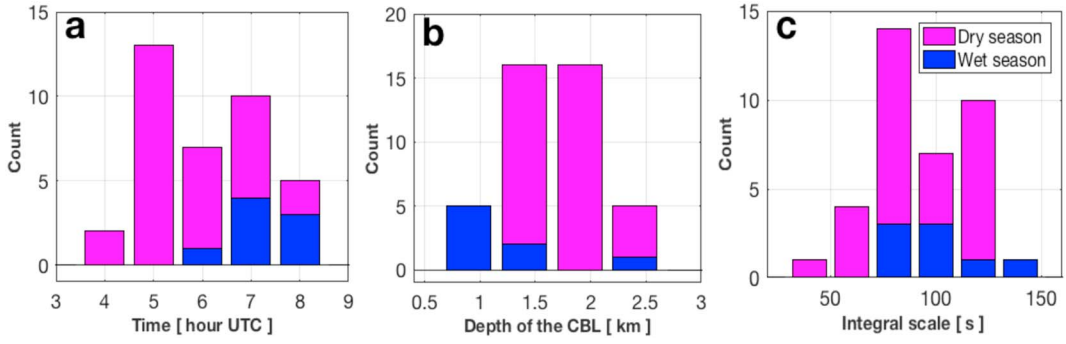

Figure 2. The distributions of (a) the center time of the 2-hr periods, (b) the depth of the convective boundary layer (CBL), and (c) integral scale at the top of the CBL. Solar noon and sunset at Darwin are 0300 UTC and 0930 UTC, respectively. The blue and magenta colors represent wet and dry season cases, respectively.

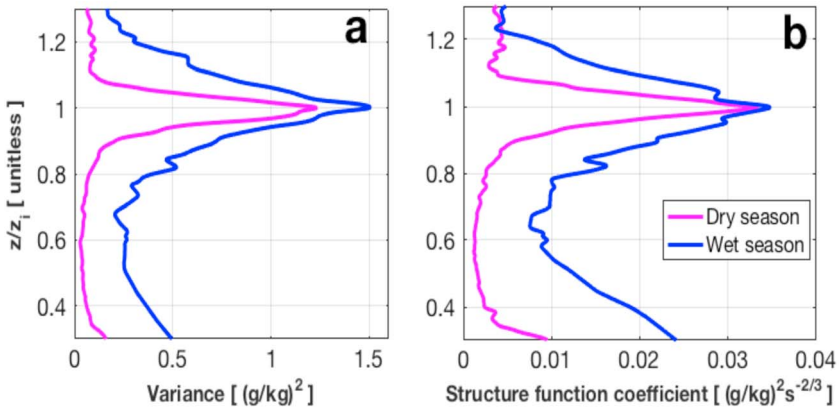

Figure 3. Median profiles of (a) atmospheric water vapor variance and (b) the coefficient of the structure function derived from the wet season (denoted in blue) and dry season (denoted in magenta) cases.

period seems to skew toward longer temporal scales and shows a larger range of IS values compared to the wet season. This can be explained by equation (5), where the IS is inversely proportional to the variance. As will be discussed in the next section, the dry season generally shows smaller variance compared to the wet season. Furthermore, we have computed the convective time scale (i.e., the ratio the CBL depth to the convective velocity scale) using the European Center for Medium Range Weather Forecast (ECMWF) Interim Re-Analysis for surface flux data and then have compared it against the IS at z_i. The result demonstrates that the convective velocity scale is significantly larger than the IS for both seasons. This finding is not surprising since z_i is greater than 1 km and w_* is less than 3 m/s for both seasons, which leads to a larger convective time scale compared to the IS at z_i.

4.3. Water Vapor Variance and Coefficient of the Structure Function

In Figure 3, we display profiles of the median of the water vapor variance and the coefficient of the structure function (i.e., the coefficient C from equation (3)) for the wet and dry seasons. Figure 3a demonstrates that the median profiles of the variance of water vapor are small both below and above the top of the CBL due to weaker variance production via vertical mixing compared to the variance production seen at z_i. The largest values of the variances at z_i are approximately 1.5 $(g/kg)^2$ for the wet season and 1.3 $(g/kg)^2$ for the dry season. A recent study by Mellado et al. (2017) used direct numerical simulations to demonstrate that the observed peak variance at z_i is due not only to large variance production at z_i, as a result of mixing of moist air from below with dry air from above, but also to weak dissipation rate at the same height. Figure 3a illustrates that the median of the water vapor variance profile is larger in the wet season than in the dry season throughout the lower troposphere. This might also be explained in terms of surface moisture flux and CBL depth. The larger water vapor variance within the CBL during the wet season might be in association with the convective scales (i.e., the ratio of surface flux to the convective velocity scale) that characterize the variance in the mixed layer (Deardorff, 1974; Sorbjan, 2005). The wet season shows larger surface moisture flux and smaller convective velocity scale resulting in higher convective scales in the season, while the dry season tends to have lower surface moisture flux and larger convective velocity scale because of deeper CBL and hence smaller convective scales. Furthermore, since the CBL depth is shallower in the wet season relative to the dry season, the length scale at which the variance created is smaller (i.e., smaller size of eddies), and this results in relatively larger destruction rate of the variance in the CBL for the wet season. However, the wet season shows larger median variance than the dry season. One possible reason is that that destruction (dissipation) rates are not large enough to counterbalance the higher variance production rates.

The variable that we computed simultaneously with the atmospheric variance by fitting the structure function shown in equation (3) was the coefficient of the structure function (C). We examined the vertical profiles of the coefficient of the structure function, which allows us to estimate the dissipation rate directly (when combined with the IS profile) as shown in Wulfmeyer et al. (2016). Figure 3b shows the profiles of the median of the coefficient of the structure function for the wet and dry seasons. As can be seen from Figures 3a and 3b,

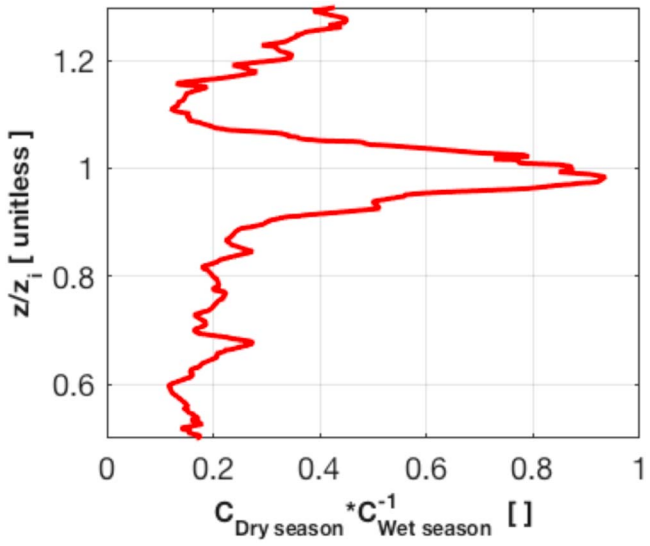

Figure 4. The ratio of the median profiles of the coefficients of the structure function for the dry season to wet season between 0.5 and 1.3 z_i.

the coefficient of the structure function follows qualitatively the same pattern with altitude as the variance. Moreover, the median of the coefficient of the structure function during the wet season is greater than during the dry season.

In order to better understand the shape of the coefficient of the structure function and what modulates it, attempts were made to link the coefficient of the structure function with the turbulence kinetic energy (TKE) dissipation rate and the molecular destruction rate of water vapor variance, as their dependence on atmospheric variables is well known. Assuming Taylor's frozen turbulence hypothesis in the inertial subrange and using the autocovariance function in the time domain, Wulfmeyer et al. (2016) defined the coefficient of the structure function for water vapor in terms of dissipation and destruction rates as

$$C = \frac{1}{2} a_q^2 \frac{\overline{N}_q}{\varepsilon^{1/3}} U^{2/3} \tag{6}$$

where the constant a_q^2 ranges between 2.8 and 3.2 (Stull, 1988), $\overline{N}_q$ is the destruction rate of water vapor variance due to molecular processes, ε is TKE dissipation rate, and U is the horizontal wind profile. Those authors furthered expressed the destruction rate of water vapor variance in terms of the variance of water vapor, variance of vertical wind, integral time, and length scales as

$$\overline{N}_q = \frac{4}{5} \frac{\overline{q'^2}\sqrt{\overline{w'^2}}}{a_q^2 \mathrm{IS}_q^{2/3} \mathrm{IS}_w^{1/3} U} = \frac{4}{5} \frac{\overline{q'^2}\sqrt{\overline{w'^2}}}{a_q^2 \mathrm{LS}_q^{2/3} \mathrm{LS}_w^{1/3}} \tag{7}$$

Combining equations (6) and (7), one finds

$$\overline{q'^2} = \left[\frac{5\varepsilon^{1/3} LS_q^{2/3} LS_w^{1/3}}{2\sqrt{\overline{w'^2}}\, U^{2/3}} \right] C \tag{8}$$

where $\overline{q'^2}$ is water vapor variance, $\overline{w'^2}$ is vertical wind variance, IS_q (LS_q) and IS_w (LS_w) are integral time (length) scales for water vapor and vertical wind, respectively.

Equation (8) illustrates that even though the peak value of the coefficient of the structure function occurs at z_i, where the variance reaches its maximum value (see Figures 3a and 3b); the latter explains only a portion of the coefficient of the structure function at z_i. Other terms such as the TKE dissipation rate, size of eddies, vertical wind variance, and horizontal wind perhaps explain the remaining variability. The verification of this hypothesis could have been done observationally if simultaneous measurements of these variables had been taken at Darwin site. Unfortunately, no such measurements were made at Darwin during this 5-year period.

We further examined the ratios of the coefficients of the structure function for dry season to wet, that is, $C_{\text{Dry season}}/C_{\text{Wet season}}$, using the median profiles of variance and the coefficient of the structure function shown in Figure 3. A linear relationship between the profiles of the coefficient of the structure function and water vapor variance was found. The result shown in Figure 4 is obtained using the slope values of the line of best fit for height range 0.5–1.3 z_i to see both within the CBL and above the top of the CBL. Figure 4 shows that the ratio is less than one both below and above z_i, suggesting that the ratio of the molecular destruction rate to the dissipation rates to the power one-third over the horizontal wind to the power two-third is much smaller in the dry season than the wet season (see equation (6)). Equation (7) illustrates that large destruction rate can be achieved through large variance and/or small size eddies (large dissipation rate). However, near the top of the CBL, the ratio is close to unity showing that the ratio of variance destruction rates to the one-third power of the dissipation rates over the horizontal wind to the power two-third is comparable for the two seasons in the entrainment zone (equation (6)). We would like to point out that the ratios obtained from the computed slopes and variances, and the coefficient of the structure function shown in Figure 3b, are in fact the same. The reason we wanted to use

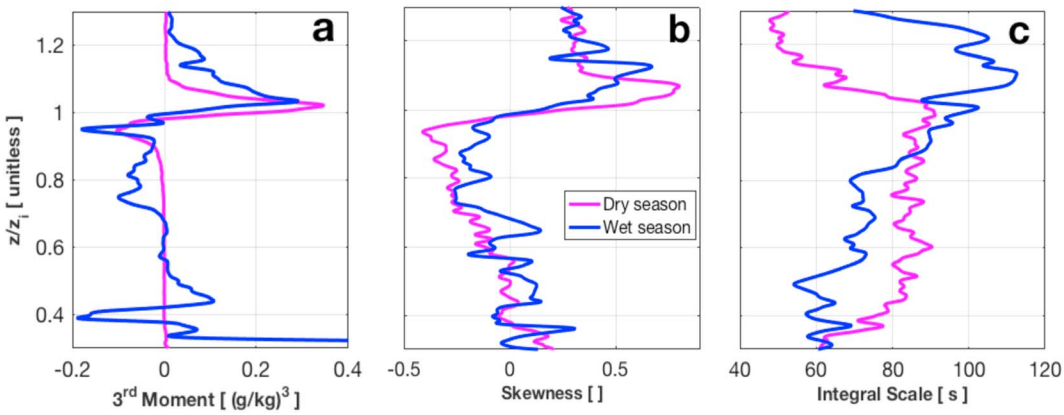

Figure 5. The median of the (a) third-order moment, (b) skewness, and (c) integral scale derived from the wet season (denoted in blue) and the dry season (denoted in magenta) cases.

the slope and variance to get the ratios is to show that the variance and coefficient of the structure function are linearly related, and then one can get the coefficient of the structure function if the variance and slope are known.

4.4. Third-Order Moment, Skewness, and Integral Scale

Figure 5 presents the median profiles of third-order moment, skewness, and IS derived from the wet and dry seasons. The dry season shows that the median of the third-order moment is very close to zero within the CBL and in the free troposphere, while it fluctuates about zero in the wet season data, which is perhaps due to a limited number of data used. Both seasons show negative skewness just below z_i and positive skewness just above z_i, with the transition from negative to positive just below the top of the CBL. The skewness, which is computed using the third and second-order moments as shown in equation (4), offers insight into the vertical transport within the CBL. The negative skewness in the upper portion of the CBL indicates descending drier air from the free troposphere into the CBL, while the positive skewness above the top of the CBL shows the moist air being lofted from the CBL into the free troposphere (Couvreux et al., 2005). The median water vapor skewness profile (Figure 5b) has the same sign as the median third-order moment with altitude. The median of the skewness in the lowest portion of the CBL, 0.4–0.7 z_i, is near zero during the dry season period, and this is perhaps due to the presence of weak moisture flux from the Earth's surface. The median normalized heights where the skewness profiles cross from negative to positive are 0.99 z_i for the wet and dry seasons (figure not shown).

Figure 5c depicts the median of the profiles of the IS for the wet and dry seasons at the TWP site. The typical value of the IS in the dry season is about 80 s between 0.4 and 1.0 z_i, while in the wet season, it tends to increase from 60 s in the lower portion of the CBL to about 100 s at the top of the CBL. The significant variability in the wet season IS might be due to limited data as mentioned earlier.

4.5. Random and Sampling Errors

In addition to the profiles of the different moments, the uncertainties in these vertical profiles were also computed. The median of the 1-sigma uncertainty profiles in IS, variance, third-order moment, and skewness are shown in Figure 6 for the wet and dry seasons. Figure 6a shows that the largest uncertainty in the IS is 8 s at 0.3 z_i and decreases with altitude approaching 1 s at 1.0 z_i. Even the peak value of the IS uncertainty is significantly smaller than the median IS value presented in Figure 5c. The median of the uncertainty in variance (Figure 6b) is largest at 0.3 z_i, where it is prone to significant error, but decreases with height becoming near zero above 0.6 z_i, which is considerably smaller than the measurements of the median values of the variance shown in Figure 3a. The medians of the uncertainty in third-order moment (Figure 6c) are near zero between 0.5–0.95 z_i and above 1.1 z_i. In the dry season, the uncertainty in the third-order moment reaches peak value of close to 0.01 $(g/kg)^3$ at 1.02 z_i but is much smaller than the measurements of the third-order moment displayed in Figure 5a. During the wet season, the uncertainty in the third-order moment shows fluctuations at the lowest altitude, where there are significant errors in addition to having a limited

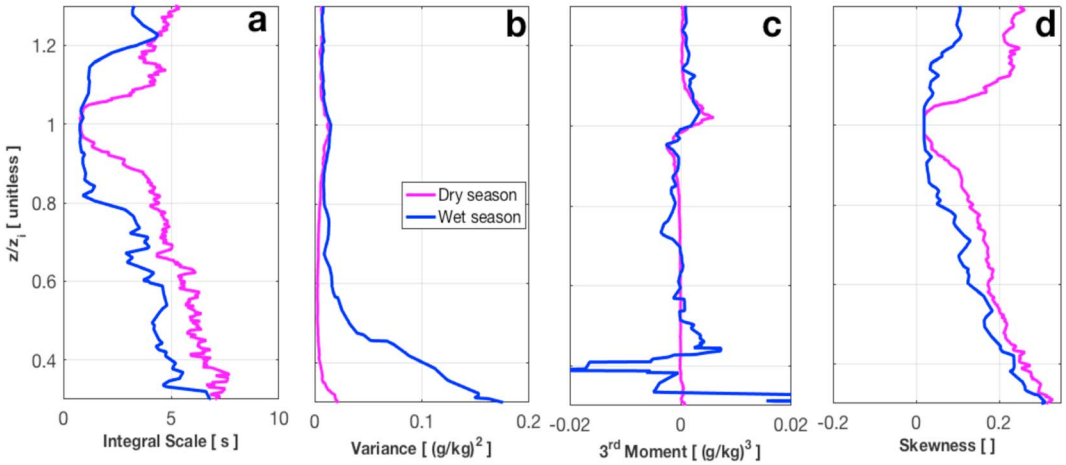

Figure 6. Median random error profiles derived from the wet season (blue) and dry season (magenta) cases for (a) integral scale, (b) variance, (c) third-order moment, and (d) skewness.

number of cases in the season. Figure 6d demonstrates that the profiles of the skewness uncertainty are small with the median values remaining less than 0.3 and approaching zero close to the top of the CBL, above which they start to increase. Overall, the computed levels of the uncertainties in the IS, variance, third-order moment, and skewness are small compared to the measured values. Furthermore, all of them show very small relative errors throughout the CBL (Figure not shown) except the skewness that reveals large relative error in the middle of the CBL during the dry season due to nearly zero values of the skewness over the same height range.

We investigated the sampling errors in water vapor variance, third-order moment, and skewness, which were computed based on the methods found in Lenschow et al. (1994) and Mann et al. (1995); the sampling error in IS is not defined. The medians of the sampling errors in the profiles of the turbulent fluctuations are shown in Figure 7. The maximum sampling error in the variance profiles occurs near the top of the CBL for both seasons (Figure 7a). However, the peak values of the median sampling errors are 6 (wet season) to 7 (dry season) times smaller than the median of the measured variance at the same altitude. The

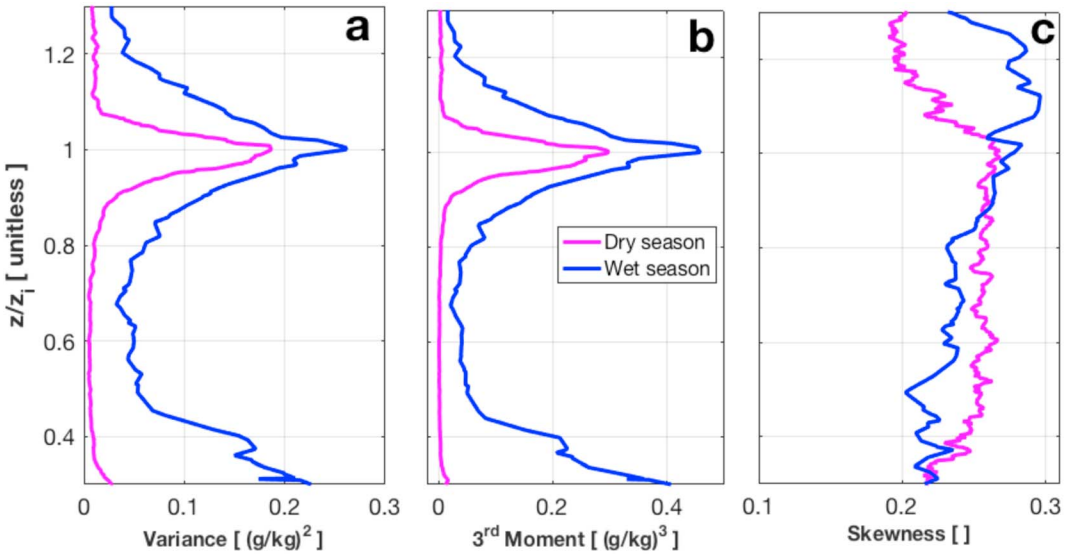

Figure 7. Median sampling uncertainty profiles derived from the wet season (blue) and dry season (magenta) cases for (a) variance, (b) third-order moment, and (c) skewness. The sampling uncertainty in integral scale is not defined.

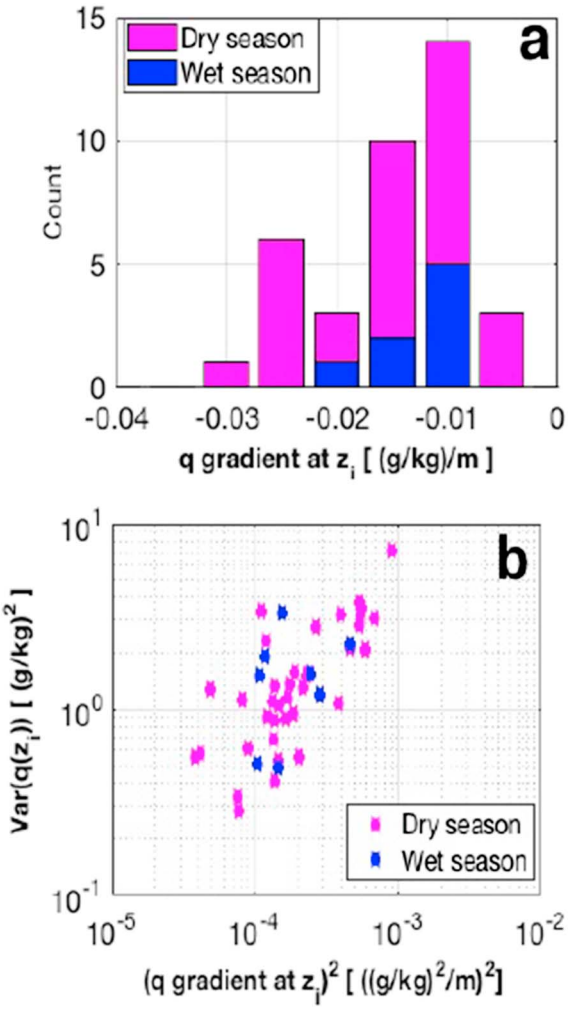

Figure 8. The distribution of the (a) vertical gradient in water vapor mixing ratio at the top of the convective boundary layer (CBL) and (b) the atmospheric variance at the top the CBL as a function of the square of the gradient of water vapor mixing ratio at the top of the CBL. The blue and magenta colors represent wet and dry seasons cases, respectively.

sampling errors in the profiles of the third-order moment (Figure 7b) also show qualitatively the same pattern as the sampling errors in variance profiles, with the maximum sampling error in the third-order moment profile at the top of the CBL. Figures 7a and 7b illustrate that the sampling errors both in the variance and third-order moment profiles are larger during the wet season than in dry season; this is particularly noticeable at the lower altitudes in the CBL. Figure 7c indicates that the median of the sampling error in the skewness profiles ranges between 0.2 and 0.3 and appears to slightly increase with altitude within the CBL during the wet season. These sampling errors could be reduced by extending the analysis periods beyond 2 hr if the CBL remained quasi-stationary and well mixed for a longer period of time.

4.6. Distribution of Variance at z_i and Its Relationships With Different Atmospheric Variables

Turner, Wulfmeyer, et al. (2014) demonstrated that the water vapor variance at the top of the CBL noticeably varied with season at the SGP site. Hence, we also examined the distribution of water vapor variance at Darwin at the top of the CBL for the two distinct seasons. Table 1 shows the 10th, 25th, 50th, 75th, and 90th percentiles of the depth of the CBL and water vapor variance at the top of the CBL derived for the wet and dry seasons. We caution that the wet season results are obtained from the limited number of cases we have from that season, whereas the dry season was reasonably well sampled. While the 25th percentile and median value of the variances at the top of the CBL are relatively larger in the wet season, the converse is true for other percentiles. Furthermore, the dry season shows relatively large variability in variance at the top of the CBL, with one case having variance at the top of the CBL as large as 7 $(g/kg)^2$. Our findings confirm Turner, Wulfmeyer, et al.'s (2014) finding that there is large variability in the variance at the top of the CBL. Furthermore, both studies show a small number of cases with very large values in variance at the top of the CBL.

Table 1 also demonstrates that the random errors and sampling uncertainties are significantly smaller than the measured variance values. The same table confirms that the depth of the CBL is deeper during the dry season, and this can be seen from all percentiles. The difference is statistically significant since the random error in estimating z_i is considered to be the vertical resolution of the Raman lidar, which is 37.5 m.

We explored the relationship between variance at the top of the CBL and the vertical gradient of water vapor mixing ratio at the same height. Numerous studies used LES models to examine the variability and structure of the CBL to establish similarity relationships that would relate geophysical variables that are predicted by numerical models (e.g., gradients in water vapor and temperature, wind speed, and shear) to the turbulent structure of the CBL (e.g., Deardorff, 1974; Neggers et al., 2007; Sorbjan, 2005). For instance, Sorbjan's (2005) large eddy simulations showed that the variance in water vapor at z_i is proportional to the square of the gradient of water vapor mixing ratio at z_i (g_i^2). We have computed g_i using the least square fit of a quadratic function to each water vapor mixing ratio profile versus altitude around the entrainment zone. We have used 11 data points for individual fitting. The gradient of water vapor mixing ratio at z_i is obtained by differentiating fitted q with respect to z and then evaluating it at z_i. The top panel of Figure 8 shows the distribution of g_i, while the bottom panel displays the relationship between the variance at z_i and g_i^2. As can be seen from Figure 8a, dry season exhibits larger gradients in water vapor mixing ratio at the top of the CBL compared to the wet season; this is also observed in Figure 1. One can perceive from Figure 8b that the dry season points

Table 2
Correlation Coefficient (r) and Its Uncertainty (Se_r) Between Variance at Three Levels (0.35 z_i, 0.6 z_i, and z_i) and Various Variables for the Dry Season (n = 37)

	Variance at					
	0.35 z_i		0.6 z_i		z_i	
Variable	r	Se_r	r	Se_r	r	Se_r
Surface sensible heat flux	−0.3	0.16	0.16	0.17	0.45	0.15
Surface latent heat flux	0.13	0.17	−0.06	0.17	−0.19	0.17
Convective velocity scale (w_*)	−0.42	0.15	0.16	0.17	0.47	0.15
Square of the gradient water vapor mixing ratio at z_i	0.03	0.17	0.61	0.13	0.83	0.09
Depth of the boundary layer	−0.41	0.15	0.14	0.17	0.37	0.16
Square of the Brunt-Vaisala frequency at z_i	−0.29	0.16	0.01	0.17	0.08	0.17
$w_*^2 \frac{g_i^2}{N_i^2}$	−0.08	0.17	0.53	0.14	0.79	0.1

are more scattered compared to the wet season, which is perhaps due to limited data we have in the wet season. The square of the water vapor gradient at z_i only explains a portion of the variance in the water vapor at z_i; other variables such as the stability and/or shear at the top of the CBL might help to explain the rest of the variability (Wulfmeyer et al., 2016).

We have computed the correlation coefficients between the square of the gradient of water vapor mixing ratio at z_i and variance at z_i; they are 0.24 ± 0.40 and 0.83 ± 0.09 for wet and dry seasons, respectively. Furthermore, the slopes of the lines of best fit were found to be 6,406 ± 1,690 and 6,223 ± 403 m^2 for wet and dry seasons, respectively. This suggests that the slopes of the regression lines during the wet and dry seasons are statistically equal. The computed slope is the constant of proportionality in Sorbjan (2005) formula that expresses the variance at z_i in terms of g_i^2 as

$$\overline{q'^2}(z_i) = \text{const} * g_i^2 \tag{9}$$

where const $= \frac{c_q w_*^2}{N_i^2}$, w_* is the convective velocity scale, N_i is the Brunt-Vaisala frequency in the interfacial layer, and c_q is an empirical constant. Hence, the computed slope during the wet and dry seasons is controlled by either one of the above parameters or both. Furthermore, equation (9) shows that the surface sensible heat flux has an impact on the computed slope since the convective velocity scale depends on the surface flux.

We have also examined the relationship between the variance at different heights and variables that are used to describe the surface and CBL turbulent processes. The variables analyzed were surface latent and sensible heat fluxes, the convective velocity scale, the gradient of water vapor mixing ratio at z_i, depth of the CBL, the Brunt-Vaisala frequency at z_i, and $w_*^2 \frac{g_i^2}{N_i^2}$. The correlations between these variables and the variance at 0.35 z_i, 0.6 z_i, and z_i were calculated and shown in Table 2.

Since there were no surface measurements of sensible and latent heat fluxes near Darwin during this 5-year period, we have used data from the ECMWF Interim Re-Analysis product (Dee et al., 2011). Three closest land surface ECMWF grid points to the Darwin site were used for this calculation. They are located within the distance of 14 km north, northeast, and southeast of the Darwin Raman lidar site. The reanalysis contains forecast surface sensible and latent heat fluxes obtained from analysis data set at 3, 6, 9, and 12-hr steps into the future with a spatial resolution of 0.125° × 0.125°. The model output data that were closest in time to the observed data were used in this analysis.

The Brunt-Vaisala frequency at z_i was computed using 10-min, 75-m resolution Raman lidar temperature data for the 2-hr time series. The ARM Raman lidar temperature data set was used in this study (ARM Climate Research Facility, 2009). The details of the derivation techniques of the atmospheric temperature profiles from the raw Raman lidar measurements and its validation can be found in Newsom, Turner, and Goldsmith (2013).

Table 2 demonstrates that variance at 0.35 z_i does not seem to be significantly influenced by surface latent heat flux (r = 0.13 ± 0.17), the square of the gradient of water vapor mixing ratio at z_i (r = 0.03 ± 0.17), or the variable that is derived from it, that is, $w_*^2 \frac{g_i^2}{N_i^2}$ (r = −0.08 ± 0.17) since the standard error of the correlation coefficients is nearly equal to or greater than the corresponding correlation coefficients. The first result is surprising, but it is probably due to the horizontal advection of water vapor, which weakens the influence of surface latent heat flux on the variance at 0.35 z_i at the TWP site. Relatively strong negative correlations between the variance at 0.35 z_i and the depth of the CBL (r = −0.41 ± 0.15), the convective velocity scale (r = −0.42 ± 0.15), surface sensible heat flux (r = −0.30 ± 0.16), and the square of the Brunt-Vaisala frequency at z_i (r = −0.29 ± 0.16) were found. This suggests that the variance at 0.35 z_i becomes smaller as the CBL gets deeper, the frequency of oscillation of air parcels about its equilibrium level of neutral buoyancy increases, and/or the surface sensible heat flux becomes larger. The former is probably related with the scaling of the variance, which is defined as the ratio of the surface flux to the convective velocity scale, and the increase

of the convective velocity scale with the depth of the CBL. The last two perhaps indicate that an increase in buoyancy frequency at z_i and surface sensible heat flux lead to large production of turbulence, which may result in strong vertical mixing and low variance. It is not surprising to see relatively strong negative correlation between the variance at 0.35 z_i and w_* since the expression for w_* contains the depth of the CBL, which shows the large negative correlation with the variance at the same height.

Relatively strong correlations of the water vapor variance at 0.6 z_i were observed with the square of the gradient of water vapor mixing ratio at z_i ($r = 0.61 \pm 0.13$) and the variable that is derived from it, that is, $w_*^2 \frac{g_i^2}{N_i^2}$ ($r = 0.53 \pm 0.14$). This demonstrates that the variance at 0.6 z_i is predominantly affected by the gradient of water vapor mixing ratio at z_i. Other variables show very small correlation coefficient values with variance at 0.6 z_i, implying that the variance at this altitude is not significantly influenced by these variables. Furthermore, the correlation coefficients are small compared to their uncertainties.

At the top of the CBL, the best correlations were obtained with the square of the gradient of water vapor mixing ratio at z_i ($r = 0.83 \pm 0.09$) and $w_*^2 \frac{g_i^2}{N_i^2}$ ($r = 0.79 \pm 0.10$), indicating that the variance at z_i is largely controlled by the gradient of water vapor maxing ratio at z_i. The depth of the CBL ($r = 0.45 \pm 0.15$) had statistically the same correlation coefficient value as the convective velocity scale ($r = 0.47 \pm 15$) and surface sensible heat fluxes ($r = 0.45 \pm 0.15$). Turner, Wulfmeyer, et al. (2014) reported the correlation coefficient values of the variance at z_i with the square of the gradient of water vapor mixing ratio at z_i, the convective velocity scale, surface latent, and sensible heat fluxes that are nearly within the standard error of the correlation coefficients found in this study.

5. Comparison of Darwin and SGP Site Profiles

As there are virtually identical Raman lidars at Darwin and the ARM SGP site in Oklahoma, a comparison of the water vapor turbulence profiles at the two sites was performed. Figure 9 compares the median profiles of water vapor mixing ratio, atmospheric variance, skewness, and IS from the two sites. The blue and magenta thick lines in Figure 9 indicate the median of profiles at Darwin for the wet and dry season periods, respectively, while the black dashed line denotes the median profile obtained from the SGP site.

Figure 9a shows that the median profiles of water vapor mixing ratio from the tropical dry season are more comparable to the SGP midlatitude site than the tropical wet season. The median profiles from the dry season and the SGP site show sharper gradient in the entrainment zone, suggesting restricted entrainment of drier air from the free troposphere into the CBL. Figure 9b displays the median profiles of the variance profiles of water vapor from the dry season, wet season, and SGP site. The wet season shows larger variance values throughout the CBL and in the free troposphere than the dry season and SGP site, indicating strong variance production in the wet season. The median variance profile of the dry season seems to agree well with the SGP observations between 0.4 and 0.75 z_i. The same figure also demonstrates that the dry season and the SGP site have similar variance values near z_i, suggesting that the thickness of the interfacial layer in the dry season is more comparable to the SGP site than the wet season.

The other quantity that has been examined in this study, which offers information regarding the vertical mixing in the entrainment zone, is skewness. Figure 9c presents the median profiles of the skewness obtained from the wet season, dry season, and SGP site. Negative and positive values of skewness are observed just below and above z_i, respectively, at both sites. Furthermore, the skewness profiles cross from negative to positive just below z_i. The TWP site shows fluctuations below 0.7 z_i in the wet season, while the dry season shows near zero values in these altitude ranges but slightly decreasing with height. However, the median skewness in the SGP site is negative within the CBL, and the observed negative skewness in the lower part of the CBL may be due to dry tongues of air from above the CBL getting mixed to these low altitudes. In general, the behavior of the median skewness profiles at the TWP site appears to be the same as the SGP site despite the difference in the values of the skewness seen below 0.6 z_i. Figure 9d shows the median of the profiles of the IS for both the TWP and SGP sites. The typical value of the IS for the TWP site dry season is 80 s, and during the TWP wet season, it ranges from 60 to 100 s. At the SGP, the median IS value is much larger than the TWP site; however, there is a significant variability in the SGP IS from the 300 cases as it ranges from less than 100 s to over 300 s.

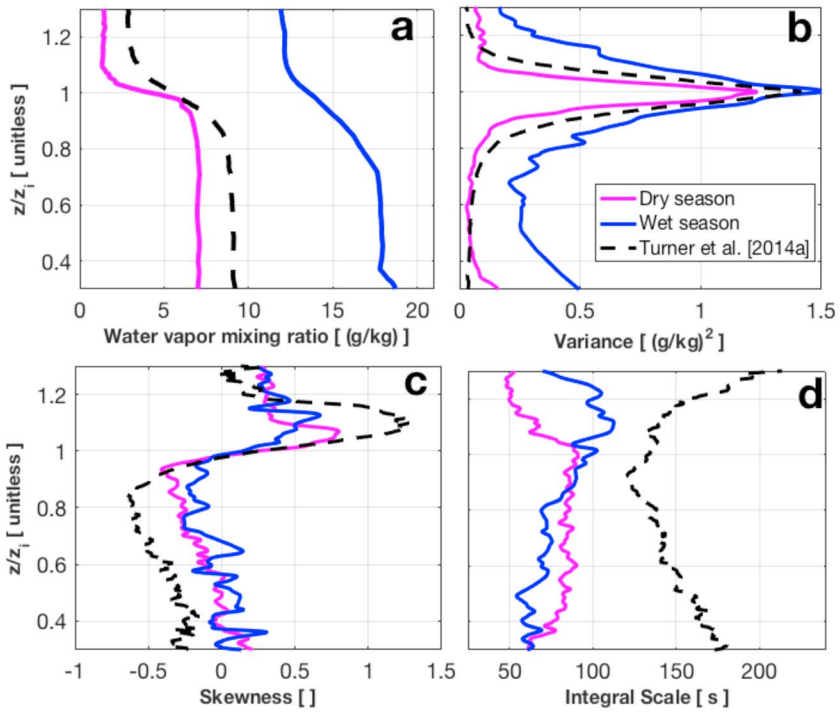

Figure 9. Comparisons of the median vertical profiles derived from Darwin and Southern Great Plains (SGP) sites. Median profiles of (a) water vapor mixing ratio, (b) atmospheric water vapor variance, (c) skewness, and (d) integral scale derived from the wet season (denoted in blue) and dry season (denoted in magenta) cases. The dashed dark lines in Figure 9 are the median profiles at the SGP site taken from Turner, Wulfmeyer, et al. (2014). The median profiles from the SGP site were computed from 300 cases, while in the Tropical Western Pacific site used 8 and 37 cases for wet and dry seasons, respectively.

Even though interesting comparison results have been obtained between the tropical wet and dry seasons at the TWP and the midlatitude SGP site, we would like to caution that the results are from a limited data set from the tropical site. This is due to the fact that cloud free, quasi-stationary, and well mixed CBL for at least a 2-hr period, which are our case selection criteria, is not a common atmospheric condition at Darwin site. This is particularly true during the wet season where we ended up with only eight cases. Thus, the statistical significance of the results especially from the wet season is limited.

6. Summary

For the first time, profiles of water vapor turbulence have been presented from a tropical site. The autocovariance technique was used to derive the profiles of variance, the coefficient of the structure function, third-order moment, skewness, and IS from 45 cases, consisting of 8 wet and 37 dry seasons events, over the 5-year Raman lidar data record period from December 2010 to December 2015. In each case, the CBL was quasi-stationary and well mixed for at least a 2-hr period in the afternoon. The results show distinct seasonal differences in the mean water vapor mixing ratios and turbulent fluctuations. The wet season is much moister, with larger mean water vapor mixing ratio values than the dry season, which is consistent with the characteristics of the seasons. The water vapor mixing ratio profiles also decrease faster above z_i in the dry season than in the wet season cases, and enhanced water vapor contents are seen in free troposphere in the wet season. The main driver of this marked seasonality difference in the profiles is both the moist maritime air masses that come from the ocean as a part of monsoonal atmospheric circulation in northern Australia and also the relatively strong mixing in the entrainment zone during the wet season. Furthermore, the median vertical profile water vapor mixing ratio in the dry season is more comparable to the SGP site than the median profile in the wet season. The CBL in the wet season is found to be relatively shallow, while it is deeper during the dry season as one would expect.

The low instrumental noise errors and high temporal and spatial resolution of the lidar's measurement allow us to compute the vertical profiles of turbulent fluctuations of second- and third-order moments throughout the CBL. Vertical profiles of the uncertainties in these profiles were derived, and the magnitudes of the errors

in the IS, variance, third-order moment, and skewness were found to be small. The IS is significantly larger than the temporal resolution of the Raman lidar water vapor data at all heights, suggesting that the lidar was able to resolve the major part of the turbulent fluctuations in the CBL.

The median profile of variance in the wet season is higher than the dry season, while the vertical profiles of the median in variance in the dry season and the SGP were found to be more comparable. The higher median variance during the wet season might be associated with the scaling of the variance, which becomes larger during the wet season due to larger surface moisture flux and smaller convective velocity scale during the wet season. The dry season shows large variability in variance at z_i, with one case having variance at the top of the CBL as much as 7 $(g/kg)^2$. This study also found a relatively strong correlation between the variance at z_i and the square of the gradient of water vapor mixing ratio at z_i; similar results were found for the SGP site (Turner, Wulfmeyer, et al., 2014). This indicates that the variance at the top of the CBL is affected by the vertical gradient of the water vapor mixing ratio at z_i, with larger values linked with the moister CBL relative to a drier free troposphere. The work also finds that the variance at 0.35 z_i is not correlated with the surface latent flux.

The vertical profile of the coefficient of the structure function, which is directly proportional to the water vapor variance and inversely proportional to the one-third power to dissipation rate, was also found to show qualitatively the same vertical pattern as the variances. Its peak value occurs at z_i, where variance is largest, not only due to large water vapor variance production at z_i but also the dissipation rate becomes small at that height. The median coefficient of the structure function in the wet season is greater than during the dry season in association with large water vapor variance production in the wet season.

The median of the vertical profile of the skewness shows a transition from negative to positive just below the top of the CBL (between 0.95 z_i and 0.99 z_i) at both the TWP and SGP sites. The negative skewness in the upper portion of the CBL indicates the descending of drier air from the free troposphere into the CBL, while the positive skewness above the top of the CBL shows the moist air being lofted from the CBL into the free troposphere. At the TWP site, the median values in skewness in the middle-to-lower portion of the CBL during the dry season are near zero, and this is perhaps due to the presence of weak moisture flux from the Earth's surface, unlike the SGP site where the skewness is negative throughout the CBL. The tropical wet season shows predominantly positive skewness below 0.6 z_i, which is probably due to either increased moisture surface flux from rainfall moistening the land surface during the wet season; the surface latent flux in the wet season is being dominated by the ocean since the winds are predominantly westerly or northwesterly, and the ARM site is close to the coast or both.

This study demonstrates the value of the continuous, long-term, high temporal, and vertical resolution observations of water vapor from the ARM Raman lidars. Such routine active remote sensing measurements of turbulent fluctuation water vapor provide valuable information that enhances our understanding of the turbulent structure of the CBL under different atmospheric conditions. The unique data set of the profiles of turbulent statistics presented here can be used for validation of the similarity relationships, which have been traditionally evaluated only by LES model simulations, and perhaps help to improve these relationships so they become generally applicable. In order to evaluate the general applicability of similarity relationships, additional water vapor turbulent statistics (ideally supported by high-resolution measurements of temperature and wind also) need to be made in other environmental conditions to supplement these observations from the TWP and the SGP. Currently, we are working on this subject by simulating the CBL using an LES model for the selected cases at the SGP and TWP sites. The different moments and ISs will be derived and compared with the lidar observations. Furthermore, we are currently working on validating the variance similarity functions in the entrainment zone using both observations and LES output, which will be written up as a separate study. Simultaneous measurements of the eddy correlation surface flux, wind shear profiles from wind profilers, and variance profile measurements of vertical motions and water vapor by Doppler and Raman lidars, respectively, provide a unique opportunity to thoroughly examine the functions used in defining the variances and validate them. The coefficients that are used in defining the functions will also be determined observationally and compared against with the values suggested by LES studies. The LES modeling studies at the SGP site will give an insight into the LES modeling at the TWP site since there were no such simultaneous measurements of the above atmospheric variables at the site. Ultimately, improvements in the parameterizations of turbulent motions in the CBL are essential for improved weather forecasts (e.g.,

Cohen et al., 2015; Ek et al., 2003; Niu et al., 2011; Shin & Hong, 2011), for regional climate projections (e.g., Milovac et al., 2016; Warrach-Sagi et al., 2013), for the dispersion of health hazardous air pollutants and greenhouse gases, and for simulating convection initiation and the formation of clouds and precipitation (e.g., Behrendt et al., 2011; Corsmeier et al., 2011; Pal, 2016). Therefore, such long-term observations of turbulence statistics water vapor will be valuable to evaluate the performance of turbulence parameterization schemes in models, and they can also be used in weather, climate, and air quality models.

Even though our focus has been studying turbulence structure during quasi-stationary clear-sky CBLs, we stress that this is only the first analysis from the 5-year Darwin lidar data set. We anticipate that there will be future studies using this data set. For example, one of our future studies will examine the turbulent structure and evolution of developing CBLs.

Acknowledgments
This work was supported by the U.S. Department of Energy Atmospheric System Research (ASR) program via grant DE-SC0014375. The data used were collected as part of the Atmospheric Radiation Measurement (ARM) program and are available from the ARM data archive at http://www.arm.gov. The detailed comments from three anonymous reviewers were greatly appreciated.

References

Albrecht, B. A., Bretherton, C. S., Johnson, D., Scubert, W. H., & Frisch, A. S. (1995). The Atlantic stratocumulus transition experiment—ASTEX. *Bulletin of the American Meteorological Society*, *76*(6), 889–904. https://doi.org/10.1175/1520-0477(1995)076%3C0889:TASTE%3E2.0.CO;2

Andrews, E., Sheridan, P. J., Ogren, J. A., & Ferrare, R. (2004). In situ aerosol profiles over the Southern Great Plains cloud and radiation test bed site: 1. Aerosol optical properties. *Journal of Geophysical Research*, *109*, D06208. https://doi.org/10.1029/2003JD004025

Angevine, W. M., Doviak, R. J., & Sorbjan, Z. (1994). Remote sensing of vertical velocity variance and surface heat flux in a convective boundary layer. *Journal of Applied Meteorology*, *33*(8), 977–983. https://doi.org/10.1175/1520-0450(1994)033%3C0977:RSOVVV%3E2.0.CO;2

Atmospheric Radiation Measurement (ARM) Climate Research Facility (2004, updated hourly). Raman LIDAR Vertical Profiles (10SRLPROFMR1TURN). 2010-12-15 to 2015-01-01, 12.425 S 130.892 E: Tropical Western Pacific (TWP) Central Facility, Darwin, Australia (C3). Compiled by C. Sivaraman and C. Flynn. Atmospheric Radiation Measurement (ARM) Climate Research Facility Data Archive: Oak Ridge, TN. Data set accessed 2016-04-08 at https://doi.org/10.5439/1027724

Atmospheric Radiation Measurement (ARM) Climate Research Facility (2009, updated hourly). Raman LIDAR Vertical Profiles (10RLPROFTEMP1NEWS). 2010-12-15 to 2014-12-31, 12.425 S 130.892 E: Tropical Western Pacific (TWP) Central Facility, Darwin, Australia (C3). Compiled by C. Sivaraman and C. Flynn. Atmospheric Radiation Measurement (ARM) Climate Research Facility Data Archive: Oak Ridge, TN. Data set accessed 2016-04-08 at https://doi.org/10.5439/1095307

Behrendt, A., Pal, S., Aoshima, F., Bender, M., Blyth, A., Corsmeier, U., et al. (2011). Observation of convection initiation processes with a suite of state-of-the-art research instruments during COPS IOP8b. *Quarterly Journal of the Royal Meteorological Society*, *137*(S1), 81–100. https://doi.org/10.1002/qj.758

Behrendt, A., Wulfmeyer, V., Hammann, E., Muppa, S. K., & Pal, S. (2015). Profiles of second to third-order moments of turbulent temperature fluctuations in the convective boundary 679 layer: First measurements with rotational Raman lidar. *Atmospheric Chemistry and Physics*, *15*(10), 5485–5500. https://doi.org/10.5194/acp-15-5485-2015

Berg, L. K., Newsom, R. K., & Turner, D. D. (2016). Year-long vertical velocity statistics derived from Doppler lidar data for the continental convective boundary layer. *Journal of Applied Meteorology and Climatology*, *56*, 2441–2454. https://doi.org/10.1175/JAMC-D-16-0359.1

Berg, L. K., & Stull, R. B. (2005). A simple parameterization coupling the convective daytime boundary layer and fair-weather cumuli. *Journal of the Atmospheric Sciences*, *62*(6), 1976–1988. https://doi.org/10.1175/JAS3437.1

Bonin, T. A., Newman, J. F., Klein, P. M., Chilson, P. B., & Wharton, S. (2016). Improvement of vertical velocity statistics measured by a Doppler lidar through comparison with sonic anemometer observations. *Atmospheric Measurement Techniques*, *9*(12), 5833–5852. https://doi.org/10.5194/amt-9-5833-2016

Bowman, D. M. J. S., Brown, G. K., Braby, M. F., Brown, J. R., Cook, L. G., Crisp, M. D., et al. (2010). Biogeography of the Australian monsoon tropics. *Journal of Biogeography*, *37*(2), 201–216. https://doi.org/10.1111/j.1365-2699.2009.02210.x

Businger, J. A., Wyngaard, J. C., Izumi, Y., & Bradley, E. F. (1971). Flux-profile relationships in the atmospheric surface layer. *Journal of the Atmospheric Sciences*, *28*(2), 181–189. https://doi.org/10.1175/1520-0469(1971)028%3C0181:FPRITA%3E2.0.CO;2

Chan, K. M., & Wood, R. (2013). The seasonal cycle of planetary boundary layer depth determined using COSMIC radio occultation data. *Journal of Geophysical Research: Atmospheres*, *118*, 12,422–12,434. https://doi.org/10.1002/2013JD020147

Cohen, A. E., Cavallo, S. M., Coniglio, M. C., & Brooks, H. E. (2015). A review of planetary boundary layer parameterization schemes and their sensitivity in simulating southeastern U.S. cold season severe weather. *Weather and Forecasting*, *30*(3), 591–612. https://doi.org/10.1175/WAF-D-14-00105.1

Cohn, S. A. (1995). Radar measurements of turbulent eddy dissipation rate in the troposphere: A comparison of techniques. *Journal of Atmospheric and Oceanic Technology*, *12*(1), 85–95. https://doi.org/10.1175/1520-0426(1995)012%3C0085:RMOTED%3E2.0.CO;2

Cooper, D. I., & Eichinger, W. E. (1994). Structure of the atmosphere in an urban planetary boundary layer from lidar and radiosonde observations. *Journal of Geophysical Research*, *99*, 22,937–22,948.

Corsmeier, U., Kalthoff, N., Barthlott, C., Aoshima, F., Behrendt, A., Di Girolamo, P., et al. (2011). Processes driving deep convection over complex terrain: A multi-scale analysis of observations from COPS IOP 9b. *Quarterly Journal of the Royal Meteorological Society*, *137*(S1), 137–155. https://doi.org/10.1002/qj.754

Couvreux, F., Guichard, F., Redelsperger, J.-L., Kiemle, C., Masson, V., Lafore, J.-P., & Flamant, C. (2005). Water-vapour velocity within a convective boundary layer assessed by large-eddy simulations and IHOP_2002 observations. *Quarterly Journal of the Royal Meteorological Society*, *131*(611), 2665–2693. https://doi.org/10.1256/qj.04.167

Deardorff, J. W. (1974). Three-dimensional numerical study of turbulence in an entraining mixed layer. *Boundary-Layer Meteorology*, *7*(2), 199–226. https://doi.org/10.1007/BF00227913

Dee, D. P., Uppala, S. M., Simmons, A. J., Berrisford, P., Poli, P., Kobayashi, S., et al. (2011). The ERA-Interim reanalysis: Configuration and performance of the data assimilation system. *Quarterly Journal of the Royal Meteorological Society*, *137*(656), 553–597. https://doi.org/10.1002/qj.828

Dehghan, A., Hocking, W. K., & Srinivasan, R. (2014). Comparisons between multiple in-situ aircraft turbulence measurements and radar in the troposphere. *Journal of Atmospheric and Solar - Terrestrial Physics*, *118*, 64–77. https://doi.org/10.1016/j.jastp.2013.10.009

Drosdowsky, W. (1996). Variability of the Australian summer monsoon at Darwin: 1957–1992. *Journal of Climate*, *9*(1), 85–96. https://doi.org/10.1175/1520-0442(1996)009%3C0085:VOTASM%3E2.0.CO;2

Ecklund, W. L., Carter, D. A., & Balsley, B. B. (1988). A UHF wind profiler for the boundary layer: Brief description and initial results. *Journal of Atmospheric and Oceanic Technology*, *5*(3), 432–441. https://doi.org/10.1175/1520-0426(1988)005%3C0432:AUWPFT%3E2.0.CO;2

Ek, M. B., Mitchell, K. E., Lin, Y., Rogers, E., Grunmann, P., Koren, V., et al. (2003). Implementation of Noah land surface model advances in the National Centres for Environmental Prediction operational mesoscale Eta model. *Journal of Geophysical Research*, *108*(D22), 8851. https://doi.org/10.1029/2002JD003296

Evans, S. M., Marchand, R. T., Ackerman, T. P., & Beagley, N. (2012). Identification and analysis of atmospheric states and associated cloud properties for Darwin, Australia. *Journal of Geophysical Research*, *117*, D06204. https://doi.org/10.1029/2011JD017010

Frehlich, R., & Sharman, R. (2010). Climatology of velocity and temperature turbulence statistics determined from radiosondes and ACARS/AMDAR data. *American Meteorological Society*, *49*, 1149–1169.

Garcia-Carreras, L., Parker, D. J., Marsham, J. H., Rosenberg, P. D., Brooks, I. M., Lock, A. P., et al. (2015). The turbulent structure and diurnal growth of the Saharan atmospheric boundary layer. *Journal of the Atmospheric Sciences*, *72*(2), 693–713. https://doi.org/10.1175/JAS-D-13-0384.1

Giez, A., Ehret, G., Schwiesow, R. L., Davis, K. J., & Lenschow, D. H. (1999). Water vapor flux measurements from ground-based vertically pointed water vapor differential absorption and Doppler lidars. *Journal of Atmospheric and Oceanic Technology*, *16*(2), 237–250. https://doi.org/10.1175/1520-0426(1999)016%3C0237:WVFMFG%3E2.0.CO;2

Goldsmith, J. E. M., Blair, F. H., Bisson, S. E., & Turner, D. D. (1998). Turn-Key Raman lidar for profiling atmospheric water vapor, clouds, and aerosols. *Applied Optics*, *37*, 4979–4990.

Holland, G. J. (1986). Interannual variability of the Australian summer monsoon at Darwin: 1952–82. *Monthly Weather Review*, *114*(3), 594–604. https://doi.org/10.1175/1520-0493(1986)114%3C0594:IVOTAS%3E2.0.CO;2

Holloway, C. E., & Neelin, J. D. (2009). Moisture vertical structure, column water vapor, and tropical deep convection. *Journal of the Atmospheric Sciences*, *66*(6), 1665–1683. https://doi.org/10.1175/2008JAS2806.1

Holton, J. R. (2004). *An introduction to dynamic meteorology* (4th ed., p. 380). Massachusetts: Elsevier Academic Press.

Kaimal, J. C., & Gaynor, J. E. (1983). The Boulder Atmospheric Observatory. *Journal of Climate and Applied Meteorology*, *22*(5), 863–880. https://doi.org/10.1175/1520-0450(1983)022%3C0863:TBAO%3E2.0.CO;2

Kiemle, C., Ehret, G., Biez, A., Davis, K. J., Lenschow, D. H., & Oncley, S. P. (1997). Estimation of the boundary layer humidity fluxes and statistics from airborne differential absorption lidar (DIAL). *Journal of Geophysical Research*, *102*, 29,189–29,203. https://doi.org/10.1029/97JD01112

Lenschow, D. H., Mann, J., & Kristensen, L. (1994). How long is long enough when measuring fluxes and other turbulence statistics? *Journal of Atmospheric and Oceanic Technology*, *11*(3), 661–673. https://doi.org/10.1175/1520-0426(1994)011%3C0661:HLILEW%3E2.0.CO;2

Lenschow, D. H., Wulfmeyer, V., & Senff, C. (2000). Measuring second- through fourth-order moments in noisy data. *Journal of Atmospheric and Oceanic Technology*, *17*(10), 1330–1347. https://doi.org/10.1175/1520-0426(2000)017%3C1330:MSTFOM%3E2.0.CO;2

Lenschow, D. H., Wyngaard, J. C., & Pennell, W. T. (1980). Mean-field and second-moment budgets in a baroclinic convective boundary layer. *Journal of the Atmospheric Sciences*, *37*(6), 1313–1326. https://doi.org/10.1175/1520-0469(1980)037%3C1313:MFASMB%3E2.0.CO;2

Long, C. N., Mather, J. H., & Ackerman, T. P. (2016). The ARM Tropical Western Pacific (TWP) sites. In *The Atmospheric Radiation Measurement (ARM) program: The first 20 years*, *Meteorological Monographs* (Vol. 57, Chap. 7, pp. 7.1–7.14). Boston, MA: American Meteorological Society. https://doi.org/10.1175/AMSMONOGRAPHS-D-15-0024.1

Mann, J., Lenschow, D. H., & Kristensen, L. (1995). Comments on "A definite approach to turbulence statistical studies in planetary boundary layers.". *Journal of the Atmospheric Sciences*, *52*(17), 3194–3196. https://doi.org/10.1175/1520-0469(1995)052%3C3194:CODATT%3E2.0.CO;2

McCaffrey, K., Bianco, L., Johnston, P., & Wilczak, J. M. (2016). Vertical velocity variance measurements from wind profiling radars. *Atmospheric Measurement Techniques Discussions*, 1–29. https://doi.org/10.5194/amt-2016-299

McCaffrey, K., Bianco, L., & Wilczak, J. M. (2016). Improved observations of turbulence dissipation, rates from wind profiling radars. *Atmospheric Measurement Techniques Discussions*, 1–23. https://doi.org/10.5194/amt-2016-322

McGrath-Spangler, E. L., & Denning, A. S. (2013). Global seasonal variations of midday planetary boundary layer depth from CALIPSO space-borne LIDAR. *Journal of Geophysical Research: Atmospheres*, *118*, 1226–1233. https://doi.org/10.1002/jgrd.50198

McNicholas, C., & Turner, D. D. (2014). Characterizing the convective boundary layer turbulence with a High Spectral Resolution Lidar. *Journal of Geophysical Research: Atmospheres*, *119*, 12,910–12,927. https://doi.org/10.1002/2014JD021867

Mellado, J. P., Puche, M., & van Heerwaarden, C. C. (2017). Moisture statistics in free convective boundary layers growing into linearly stratified atmospheres. *Quarterly Journal of the Royal Meteorological Society*, *143*(707), 2403–2419. https://doi.org/10.1002/qj.3095

Milovac, J., Warrach-Sagi, K., Behrendt, A., Späth, F., Ingwersen, J., & Wulfmeyer, V. (2016). Investigation of PBL schemes combining the WRF model simulations with scanning water vapor DIAL measurements. *Journal of Geophysical Research: Atmospheres*, *121*, 624–649. https://doi.org/10.1002/2015JD023927

Monin, A. S., & Yaglom, A. M. (1979). *Statistical fluid mechanics* (p. 874). Cambridge, MA: MIT Press.

Muppa, S. K., Behrendt, A., Späth, F., Wulfmeyer, V., Metzendorf, S., & Riede, A. (2016). Turbulent humidity fluctuations in the convective boundary layer: Case studies using water vapour differential absorption lidar measurements. *Boundary-Layer Meteorology*, *158*(1), 43–66. https://doi.org/10.1007/s10546-015-0078-9

Murakami, T., Iwashima, T., & Nakasawa, T. (1984). Heat, moisture, and vorticity budget before and after the onset of the 1978–79 Southern Hemisphere summer monsoon. *Journal of the Meteorological Society of Japan*, *62*(1), 69–87. https://doi.org/10.2151/jmsj1965.62.1_69

Murakami, T., & Sumi, A. (1982). Southern Hemisphere summer monsoon circulation during the 1978–79 WMONEX. Part II: Onset, active and break monsoons. *Journal of the Meteorological Society of Japan*, *60*, 649–671.

Neggers, R. A. J., Stevens, B., & Neelin, J. D. (2007). Variance scaling in shallow-cumulus-topped mixed layers. *Quarterly Journal of the Royal Meteorological Society*, *133*(628), 1629–1641. https://doi.org/10.1002/qj.105

Neves, T. T. d. A. T., & Fisch, G. (2015). The daily cycle of the atmospheric boundary layer heights over pasture site in Amazonia, American. *Journal of Environmental Engineering*, *5*(1A), 39–44. https://doi.org/10.5923/s.ajee.201501.06

Newsom, R. K., Turner, D. D., & Goldsmith, J. E. M. (2013). Long-term evaluation of temperature profiles measured by an operational Raman lidar. *Journal of Atmospheric and Oceanic Technology*, *30*(8), 1616–1634. https://doi.org/10.1175/JTECH-D-12-00138.1

Newsom, R. K., Turner, D. D., Mielke, B., Clayton, M., Ferrare, R. A., & Sivaraman, C. (2009). The use of simultaneous analog and photon counting detection for Raman lidar. *Applied Optics*, *48*(20), 3903–3914. https://doi.org/10.1364/AO.48.003903

Niu, G.-Y., Yang, Z.-L., Mitchell, K. E., Chen, F., Ek, M. B., Barlage, M., et al. (2011). The community Noah land surface model with multiparameterization options (Noah-MP): 1. Model description and evaluation with local-scale measurements. *Journal of Geophysical Research*, *116*, D12109. https://doi.org/10.1029/2010JD015139

Pal, S. (2016). On the factors governing water vapor turbulence profiles in the convective boundary layer over land: Concept and data analyses methodology using ground-based lidar measurements. *Science of the Total Environment*, *554-555*, 17–25. https://doi.org/10.1016/j.scitotenv.2016.02.147

Pope, M., Jakob, C., & Reeder, M. J. (2008). Convective systems of the north Australian monsoon. *Journal of Climate*, *21*(19), 5091–5112. https://doi.org/10.1175/2008JCLI2304.1

Shin, H. H., & Hong, S.-Y. (2011). Intercomparison of planetary boundary-layer parameterizations in the WRF model for a single day from CASES-99. *Boundary-Layer Meteorology*, *139*(2), 261–281. https://doi.org/10.1007/s10546-010-9583-z

Sisterson, D. L., Peppler, R. A., Cress, T. S., Lamb, P. J., & Turner, D. D. (2016). The ARM Southern Great Plains (SGP) site. In *The Atmospheric Radiation Measurement (ARM) program: The first 20 years*, *Meteorological Monographs* (Vol. 57, Chap. 6, pp. 6.1–6.14). Boston, MA: American Meteorological Society. https://doi.org/10.1175/AMSMONOGRAPHS-D-16-0004.1

Sorbjan, Z. (2005). Statistics of scalar fields in the atmospheric boundary layer based on large-eddy simulations. Part 1: Free convection. *Boundary-Layer Meteorology*, *116*(3), 467–486. https://doi.org/10.1007/s10546-005-0907-3

Strauch, R. G., Merritt, D. A., Moran, K. P., Earnshaw, K. B., & Van de Kamp, D. (1984). The Colorado Wind-Profiling Network. *Journal of Atmospheric and Oceanic Technology*, *1*(1), 37–49. https://doi.org/10.1175/1520-0426(1984)001%3C0037:TCWPN%3E2.0.CO;2

Stull, R. B. (1988). *An introduction to boundary layer meteorology*. *Atmospheric and Oceanographic Sciences Library* (Vol. 13, p. 301). Dordrecht, Netherlands: Springer.

Stull, R. B., Santoso, E., Berg, L., & Hacker, J. (1997). Boundary layer experiment 1996 (BLX96). *Bulletin of the American Meteorological Society*, *78*(6), 1149–1158. https://doi.org/10.1175/1520-0477(1997)078%3C1149:BLEB%3E2.0.CO;2

Tompkins, A. M. (2002). A prognostic parameterization for the subgrid-scale variability of water vapor and clouds in large-scale models and its use to diagnose cloud cover. *Journal of the Atmospheric Sciences*, *59*(12), 1917–1942. https://doi.org/10.1175/1520-0469(2002)059%3C1917:APPFTS%3E2.0.CO;2

Troup, A. J. (1961). Variations in upper tropospheric flow associated with the onset of the Australian summer monsoon. *Indian Journal of Meteorology & Geophysics*, *12*, 217–230.

Turner, D. D., Ferrare, R. A., Wulfmeyer, V., & Scarino, A. J. (2014). Aircraft evaluation of ground-based Raman lidar water vapor turbulence profiles in convective mixed layers. *Journal of Atmospheric and Oceanic Technology*, *31*(5), 1078–1088. https://doi.org/10.1175/JTECH-D-13-00075-1

Turner, D. D., & Goldsmith, J. E. M. (1999). Twenty-four-hour Raman lidar water vapor measurements during the Atmospheric Radiation Measurement program's 1996 and 1997 water vapor intensive observation periods. *Journal of Atmospheric and Oceanic Technology*, *16*(8), 1062–1076. https://doi.org/10.1175/1520-0426(1999)016%3C1062:TFHRLW%3E2.0.CO;2

Turner, D. D., Goldsmith, J. E. M., & Ferrare, R. A. (2016). Development and applications of the ARM Raman lidar. In *The Atmospheric Radiation Measurement (ARM) program: The first 20 years*, *Meteorological Monographs* (Vol. 57, Chap. 13, pp. 13.1–13.18). Boston, MA: American Meteorological Society. https://doi.org/10.1175/AMSMONOGRAPHS-D-15-0026.1

Turner, D. D., Wulfmeyer, V., Berg, L. K., & Schween, J. H. (2014). Water vapor turbulence profiles in stationary continental convective mixed layers. *Journal of Geophysical Research: Atmospheres*, *119*, 11,151–11,165. https://doi.org/10.1002/2014JD022202

van Ulden, A. P., & Wieringa, J. (1996). Atmospheric boundary layer research at Cabauw. *Boundary-Layer Meteorology*, *78*(1-2), 39–69. https://doi.org/10.1007/BF00122486

Van Weverberg, K., Boutle, I. A., Morcrette, C. J., & Newsom, R. K. (2016). Towards retrieving critical relative humidity from ground-based remote-sensing observations. *Quarterly Journal of the Royal Meteorological Society*, *142*, 2867–2881. https://doi.org/10.1002/qj.2874

Vogelmann, A. M., McFarquhar, G., Ogren, J. A., Turner, D. D., Comstock, J. M., Feingold, G., et al. (2012). RACORO extended-term aircraft observations of boundary layer clouds. *Bulletin of the American Meteorological Society*, *93*(6), 861–878. https://doi.org/10.1175/BAMS-D-11-00189.1

Warrach-Sagi, K., Schwitalla, T., Wulfmeyer, V., & Bauer, H. S. (2013). Evaluation of a climate simulation based on the WRF-NOAH model system: Precipitation in Germany. *Climate Dynamics*, *41*(3-4), 755–774. https://doi.org/10.1007/s00382-013-1727-7

White, A. B., Fairall, C. W., & Thompson, D. W. (1991). Radar observations of humidity variability in and above the marine atmospheric boundary layer. *Journal of Atmospheric and Oceanic Technology*, *8*(5), 639–658. https://doi.org/10.1175/1520-0426(1991)008%3C0639:ROOHVI%3E2.0.CO;2

Whiteman, D. N., Demoz, B., Di Girolamo, P., Comer, J., Veselovskii, I., Evans, K., et al. (2006). Raman water vapor lidar measurements during the International H2O Project. I: Instrumentation and analysis techniques. *Journal of Atmospheric and Oceanic Technology*, *23*, 157–169. https://doi.org/10.1175/JTECH1838.1

Wilczak, J. M., & Tillman, J. E. (1980). The three-dimensional structure of convection in the atmospheric surface layer. *Journal of the Atmospheric Sciences*, *37*(11), 2424–2443. https://doi.org/10.1175/1520-0469(1980)037%3C2424:TTDSOC%3E2.0.CO;2

Williams, A. G., & Hacker, J. M. (1992). The composite shape and structure of coherent eddies in the convective boundary layer. *Boundary-Layer Meteorology*, *61*(3), 213–245. https://doi.org/10.1007/BF02042933

Wilson, R., Dalaudier, F., & Luce, H. (2011). Can one detect small-scale turbulence from standard meteorological radiosondes? *Atmospheric Measurement Techniques*, *4*(5), 795–804. https://doi.org/10.5194/amt-4-795-2011

Wulfmeyer, V. (1999a). Investigation of turbulent processes in the lower troposphere with water vapor DIAL and radar-RASS. *Journal of the Atmospheric Sciences*, *56*(8), 1055–1076. https://doi.org/10.1175/1520-0469(1999)056%3C1055:IOTPIT%3E2.0.CO;2

Wulfmeyer, V. (1999b). Investigations of humidity skewness and variance profiles in the convective boundary layer and comparison of the latter with large eddy simulation results. *Journal of the Atmospheric Sciences*, *56*(8), 1077–1087. https://doi.org/10.1175/1520-0469(1999)056%3C1077:IOHSAV%3E2.0.CO;2

Wulfmeyer, V., Behrendt, A., Sorbian, Z., Turner, D. D., & Hardesty, R. M. (2016). Determination of convective boundary layer entrainment fluxes, dissipation rates, and the molecular destruction of variances: Theoretical description and a strategy for its confirmation with a Novel Lidar System Synergy. *Journal of the Atmospheric Sciences*, *73*(2), 667–692. https://doi.org/10.1175/JAS-D-14-0392.1

Wulfmeyer, V., Pal, S., Turner, D. D., & Wagner, E. (2010). Can water vapor Raman lidar resolve profiles of turbulent variables in the convective boundary layer? *Boundary-Layer Meteorology*, *136*(2), 253–284. https://doi.org/10.1017/s10546-010-9494-z